*Progress in Propulsion Physics* **11** (2019) 177-194
https://doi.org/10.1051/eucass/201911177

# LARGE-EDDY SIMULATION OF TRANSCRITICAL LIQUID OXYGEN / METHANE JET FLAMES

**H. Müller*** **and M. Pfitzner**

Institute for Thermodynamics, Universität der Bundeswehr München
39 Werner-Heisenberg-Weg, Neubiberg 85577, Germany

A numerical method to perform large-eddy simulations (LES) of nonpremixed liquid oxygen / methane ($LOx/CH_4$) combustion at supercritical pressures is presented and the computational results are compared with available experimental data. The injection conditions of the considered test case resemble those in typical liquid-propellant rocket engines (LRE). Thermodynamic nonidealities are modeled using the Peng–Robinson (PR) equation of state (EoS) in conjunction with a novel volume-translation method to correct deficiencies in the transcritical regime. The resulting formulation is more accurate than the standard cubic EoS's without deteriorating their good computational efficiency. The real-gas thermodynamics model is coupled with the steady laminar flamelet model (SLFM) for turbulent nonpremixed combustion to incorporate chemical reactions at reasonable computational cost in the LES. A reduced reaction mechanism, which is validated with respect to the full mechanism, is used to generate a flamelet library. A comparison of the LES result with available $OH^*$ measurements shows that important flow features are well predicted.

## 1 INTRODUCTION

Today's main stage LRE typically operate at supercritical pressures, i. e., at chamber pressures that exceed the critical pressure of the propellants, and at cryogenic injection temperatures. One or both propellants are thus injected at near-critical conditions and mixing, ignition, and combustion are largely affected by nonideal thermodynamic effects. In particular, the thermodynamic- and transport properties, e. g., density, enthalpy, and viscosity, are highly nonlinear functions of temperature and pressure. Moreover, the experiments [1, 2] showed that the surface tension between liquid and vapor is diminished at sufficiently high pressures and mixing is characterized by continuous-phase diffusion

*Now at: MTU Aero Engines AG, 665 Dachauer Straße, München 80995, Germany.

rather than by two-phase spray atomization. In these diffusion mixing layers, the fluid properties change drastically and the density may vary by two orders of magnitude within a few micrometers.

Such configurations pose a serious challenge for numerical as well as for experimental studies. At the same time, their investigation is important to better understand the involved processes and to develop tools that help in the design of LREs, but also of other high-pressure combustion devices, such as novel Diesel motors or gas turbines. The topic received considerable attention in the last decade and several valuable experiments were carried out. Thorough overviews are given, for instance, by Oschwald *et al.* [3] and Chehroudi [4] focussing on the joint work of the U.S. Air Force Research Labratory (AFRL) and the German Aerospace Center (DLR) as well as by Habiballah *et al.* [5] focusing on the Mascotte testing facility. Along with the better understanding that has been generated by the experimental efforts, several groups developed models and numerical tools to perform simulations of near-critical mixing and combustion allowing for a detailed view on the flow. Among the first to conduct LES of supercritical injection were Oefelein and Yang [6] and later Zong *et al.* [7] as well as Oefelein [8]. These studies showed that the accurate treatment of thermodynamic nonidealities are key to obtain realistic numerical representations. However, accuracy comes at the cost of numerical effort and a compromise has to be made in order to keep the computational effort manageable. Here, Matheis *et al.* [9] identified and compared various volume-translation methods [10, 11] for cubic EoS's, such as PR [12] or Soave–Redlich–Kwong (SRK) [13]. These methods have the advantage to improve the predictive quality of cubic EoS's for near-critical conditions without a significant degradation of their good computational performance. In the present work, the volume-translation method of Abudour *et al.* [14], which is based on the work of Chou and Prausnitz [15], has been employed. This method was already used for LES of supercritical nitrogen injection [16] as well as of coaxial liquid nitrogen / gaseous hydrogen ($LN_2/GH_2$) injection [17].

In the present work, the focus is on simulating the injection and combustion of LOx/$GCH_4$ (gaseous $CH_4$), following the experimental operating conditions G2 of Singla *et al.* [18]. An additional subject that needs to be addressed is the choice of an appropriate combustion model for this configuration. In previous LES studies of this test case, Guézennec *et al.* [19] employed a reduced reaction mechanism accounting for finite-rate chemistry, while Schmitt *et al.* [20] made the assumption of infinitely fast chemistry and used a single-step reaction to calculate the reaction rates. This assumption was also made by Cutrone *et al.* [21] as well as by Kim *et al.* [22] who simulated the test case of Singla *et al.* [18] using a Reynolds-averaged Navier–Stokes (RANS) flamelet model. The numerical results in all these studies are in good agreement with the experimental data. In the present work, we employ the SLFM for LES [23, 24] using a presumed $\beta$-shape probability density function (PDF) for the subgrid-scale (SGS) fluctuations. The choice is supported by the comparative study of Zong *et al.* [25], who

showed that the SLFM performed better than alternative combustion closures for a splitter plate configuration at conditions that were similar to those in experiments by Singla *et al.* Furthermore, Ribert *et al.* [26] showed that the chemical consumption rates scale as the square-root of pressure and the *fast-chemistry* assumption, which is a precondition for the SLFM, appears to be appropriate for the present high-pressure configuration.

# 2 NUMERICAL AND PHYSICAL MODELING

## 2.1 Large-Eddy Simulation Equations

In LES, only the large-scale turbulent fluctuations are resolved while fluctuations on SGS level have to be modeled. The threshold between unresolved and resolved scale is determined by a certain filter width which is the local cell size in the present work. Filtering the Navier–Stokes equations leads to the filtered LES equations for mass, momentum, and energy (cf. Garnier *et al.* [27]).

As mentioned before, the flamelet concept [24] was employed to avoid the computational cost of solving a complex chemistry kinetics mechanism. The flame structure in the turbulent flow field is represented by three parameters: the scalar dissipation rate $\tilde{\chi}$, the resolved mixture fraction $\tilde{f}$, and its subgrid variance $\widetilde{f''^2}$. The scalar dissipation is modeled with an algebraic equation, whereas the mixture fraction and its variance are computed by solving a transport equation. For $\widetilde{f''^2}$, in particular, the authors follow the formulation of Kemenov *et al.* [28]. Thus, the system of governing equations for a Newtonian fluid takes the following form:

$$\frac{\partial \bar{\rho}}{\partial t} + \frac{\partial \left(\bar{\rho}\tilde{u}_i\right)}{\partial x_i} = 0\,; \tag{1}$$

$$\frac{\partial \left(\bar{\rho}\tilde{u}_i\right)}{\partial t} + \frac{\partial \left(\bar{\rho}\tilde{u}_i\tilde{u}_j\right)}{\partial x_j} = -\frac{\partial \bar{p}}{\partial x_i} + \frac{\partial}{\partial x_j}\left(2\left(\bar{\mu}+\mu_e\right)\left(\tilde{S}_{ij} - \frac{1}{3}\,\tilde{S}_{kk}\delta_{ij}\right)\right)\,; \tag{2}$$

$$\frac{\partial \left(\bar{\rho}\tilde{h}\right)}{\partial t} + \frac{\partial \left(\bar{\rho}\tilde{u}_i\tilde{h}\right)}{\partial x_i} = \frac{\partial \overline{p}}{\partial t} + \tilde{u}_i\frac{\partial \overline{p}}{\partial x_i} + \frac{\partial}{\partial x_i}\left(\left(\bar{\lambda} + c_p\frac{\mu_e}{\mathrm{Pr}_t}\right)\frac{\partial \tilde{T}}{\partial x_i}\right)\,; \tag{3}$$

$$\frac{\partial \left(\bar{\rho}\tilde{f}\right)}{\partial t} + \frac{\partial \left(\bar{\rho}\tilde{u}_i\tilde{f}\right)}{\partial x_i} = \frac{\partial}{\partial x_i}\left(\left(\frac{\bar{\mu}}{\mathrm{Sc}} + \frac{\mu_e}{\mathrm{Sc}_t}\right)\frac{\partial \tilde{f}}{\partial x_i}\right)\,; \tag{4}$$

$$\frac{\partial \left(\bar{\rho}\widetilde{f''^2}\right)}{\partial t} + \frac{\partial \left(\bar{\rho}\tilde{u}_i\widetilde{f''^2}\right)}{\partial x_i} = \frac{\partial}{\partial x_i}\left(\left(\frac{\bar{\mu}}{\mathrm{Sc}} + \frac{\mu_e}{\mathrm{Sc}_t}\right)\frac{\partial \widetilde{f''^2}}{\partial x_i}\right) - 2\bar{\rho}\tilde{\chi} + 2\left(\frac{\bar{\mu}}{\mathrm{Sc}} + \frac{\mu_e}{\mathrm{Sc}_t}\right)\left(\frac{\partial \tilde{f}}{\partial x_i}\right)^2 \tag{5}$$

where a bar $\bar{\star}$ denotes the finite-volume filter and a tilde denotes Favre-filtering, i. e., $\tilde{\star} = \overline{\rho\star}/\bar{\rho}$; $x_i$ are the Cartesian coordinates; $t$ is the time; $\bar{\rho}$ is the density; $\tilde{u}_i$ is the velocity component in direction $i$; $\mu$ and $\mu_e$ are the molecular and the eddy viscosity, respectively; $\lambda$ is the thermal conductivity; and $\tilde{S}_{ij}$ represents the symmetric stress tensor,

$$\tilde{S}_{ij} = \frac{1}{2}\left(\frac{\partial \tilde{u}_i}{\partial x_j} + \frac{\partial \tilde{u}_j}{\partial x_i}\right).$$

In the momentum equation (2), the Boussinesq eddy-viscosity assumption is implied, i. e., the subgrid stress tensor can be written as

$$\tau_{ij} = \bar{\rho}\left(\widetilde{u_i u_j} - \tilde{u}_i\tilde{u}_j\right) = 2\mu_e\left(\tilde{S}_{ij} - \frac{1}{3}\,\tilde{S}_{kk}\delta_{ij}\right) - \frac{2}{3}\,\bar{\rho}k\delta_{ij}.$$

The eddy viscosity $\mu_e$ is calculated using the SGS turbulence model of Vreman [29]. The diffusion of mixture fraction and of mixture fraction variance (Eqs. (4) and (5)) is modeled using the standard gradient diffusion assumption with the diffusion coefficient being connected with the viscosity through the molecular and turbulent Schmidt number. These are set constant to $\mathrm{Sc} = 1.0$ and $\mathrm{Sc}_t = 0.7$, respectively. The turbulent Prandtl number in the enthalpy equation is set to $\mathrm{Pr}_t = 0.7$. The scalar dissipation rate in Eq. (5) is decomposed into a resolved and an SGS contribution:

$$2\bar{\rho}\tilde{\chi} = 2\frac{\tilde{\mu}}{\mathrm{Sc}}\left(\frac{\partial \tilde{f}}{\partial x_i}\right)^2 + C_\chi\frac{\mu_e}{\mathrm{Sc}_t}\frac{\widetilde{f''^2}}{\Delta^2}. \tag{6}$$

Here, $\Delta$ is the local filter size and the model constant $C_\chi$ is set to 2.

In the present work, a Pressure Implicit with Splitting of Operators (PISO) algorithm [30, 31] has been employed. Instead of solving the continuity equation (1) directly, the discretized momentum equation is used to derive a pressure evolution equation, which guarantees mass conservation. This has the advantage that stiff equation systems, especially for low Mach number flows, are avoided and the computation can be run using larger time steps. However, several modifications are necessary to consistently incorporate real-gas thermodynamics models into the standard PISO approach. For details, refer to the work of Jarczyk and Pfitzner [32].

### 2.2 Real-Gas Thermodynamics

The thermodynamic model is based on the mixture PR EoS [12]:

$$p = \frac{RT}{v_{\mathrm{PR}} - b_m} - \frac{a_m}{v_{\mathrm{PR}}^2 + 2v_{\mathrm{PR}}b_m - b_m^2} \tag{7}$$

where $v_{\mathrm{PR}}$ is the molar volume of the mixture; $T$ is the temperature; and $R$ is the molar gas constant. Intermolecular attractive forces are described by the temperature dependent function $a_m$ and the reduction of free volume due to the finite volume of the molecules is taken into account by $b_m$. The mixing rules for these parameters are taken from the work of Harstad *et al.* [10]. The PR EoS is an adequate choice for temperatures above and close to the critical temperature; however, in the transcritical regime, considerable deviations from experimental data can be observed [11]. Therefore, in the present work, the authors employ the volume-translation method of Abudour *et al.* [14] (PR-VTA), who proposed a generalized form of the method of Chou and Prausnitz [15] that considerably improves the accuracy of the density prediction at minimal extra computational cost. The basic principle is to shift the thermodynamic state of the fluid along its volume axis keeping pressure and temperature constant. The corrected molar volume

$$v_m = v_{\mathrm{PR}} + c_m + \delta_{c_m} \frac{0.35}{0.35 + d_m}$$

is the sum of the contribution from the PR EoS $v_{\mathrm{PR}}$ and the volume correction. The term $\delta_{c_m}$ accounts for the deviation of the critical compressibility factor $Z_c$ obtained from the PR EoS and $c_m$ can be computed as

$$c_m = \frac{RT_{c,m}}{p_{c,m}} \left( c_{1,m} - (0.004 + c_{1,m})\, e^{-2d_m} \right)$$

with

$$c_{1,m} = \sum x_i c_{1,i}\,, \qquad c_{1,i} = 0.4266 Z_{c,i} - 0.1101$$

where $Z_{c,i}$ and $x_i$ are the critical compressibility factor and the mole fraction of specie $i$, respectively. The dimensionless distance function between the critical locus and the pressure–density isotherm is

$$d_m = -\frac{v_{\mathrm{PR}}^2}{RT_{c,m}} \left. \frac{\partial p}{\partial v_{\mathrm{PR}}} \right|_T .$$

Note that in the original formulation of Abudour *et al.* [14], $d_m$ contains an additional term to satisfy the intrinsic stability criterion for mixtures. This term is computationally expensive and limits the model's applicability to binary mixtures. Therefore, in the present work, it is neglected since in reacting flows, the mixed state features high temperatures diminishing the effect of the volume-translation.

The caloric properties, e. g., heat capacities and enthalpy, are calculated using the departure function formalism. The quantity of interest is decomposed into an ideal contribution which is calculated at a low reference pressure using NASA polynomials [33] and a pressure-dependent departure function. More details are given, for instance, by Poling *et al.* [34]. Note that it was not possible to find

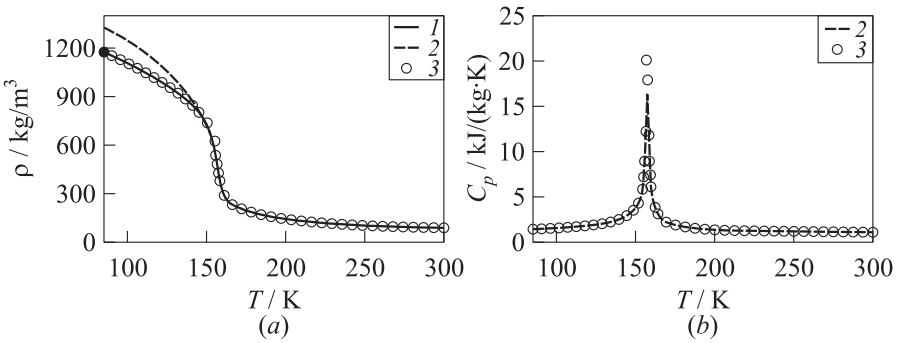


**Figure 1** Verification of the real-gas thermodynamics model for $O_2$ at $p = 5.61$ MPa: ($a$) density; ($b$) constant pressure heat capacity, *1* — PR-VTA EoS; *2* — PR EoS; and *3* — NIST chemistry webbook [36]

an analytical solution for the departure function when the volume-translation method is considered. Therefore, the uncorrected PR EoS has been used in the evaluation of the caloric properties. This inconsistency is tolerated for the benefit of a highly accurate thermal EoS (cf. Matheis *et al.* [9] for details). The viscosity and the thermal conductivity are modeled using the empirical correlation for dense fluids of Chung *et al.* [35].

Figure 1$a$ demonstrates the effect of the volume-translation method on the density prediction for $O_2$ at $p = 5.61$ MPa. While the uncorrected density deviates from the reference data of the NIST [36] for temperatures below 150 K, the density obtained with PR-VTA is in good agreement with the reference data over the entire temperature range considered in the present work. In particular, for the oxidizer injection condition ($T_{O_2} = 85$ K and $p = 5.61$ MPa) of the test case presented later on, the deviation from NIST is 10.33% for the uncorrected PR EoS and only 0.005% for the PR-VTA EoS. Figure 1$b$ shows the constant pressure heat capacity $c_p$. Note that only the PR EoS result is shown, since the volume translation of Abudour *et al.* [14] could not be considered in the evaluation of the caloric properties for the reasons mentioned above.

### 2.3 Combustion Model

As mentioned earlier, the SLFM for turbulent nonpremixed combustion [23, 24] was employed to cut the cost of solving the chemistry kinetics along with the transport equations. The concept is based on the view of the turbulent flame as an ensemble of small laminar diffusion flames, generally referred to as flamelets. The underlying assumption is that the characteristic chemical time scales are small compared to the turbulent time scales (high Damköhler number). Con-

sidering that the reaction speed scales with the pressure [26, 37], this assumption is justified for the present test case which features a chamber pressure of $p \approx 5.61$ MPa. In particular, the strained diffusion flame calculations presented below show that flame extinction occurs at scalar dissipation rates in the order of $6 \cdot 10^5$ 1/s while the maximum values of $\tilde{\chi}$ obtained in the LES are two orders of magnitude smaller. Another condition for the validity of the SLFM is that turbulent vortices do not perturb the inner structure of the flame, i. e., the flame thickness is sufficiently small compared to the turbulent length scales (small turbulent Reynolds number). The main advantage of the flamelet approach is that the flamelets, which describe the local structure of the turbulent flame, are coupled to the turbulent flow by only a few parameters, i. e., the mixture fraction, its variance, and the scalar dissipation rate. The chemistry kinetics can thus be handled separately from the turbulent flow. This feature is used to calculate the flamelets in a preprocessing step and store them in look-up tables which are accessed during the LES to retrieve the local species composition.

It is common practice in the flamelet context to obtain the thermodynamic properties from the flamelet library. However, in order to account for pressure variations, we follow the recommendation of Lacaze and Oefelein [38] and calculate the thermodynamic state of the fluid according to the result of the energy equation (3) and the tabulated species composition using the real-gas thermodynamics model presented in the previous subsection.

The reduced methane oxidation mechanism of Jones and Lindstedt [39] has been used with additional reactions that account for dissociation of water and oxygen as proposed by Frassoldati *et al.* [40] (Table 1). The reduced mechanism contains 9 species and 6 reactions and is thus considerably smaller than the full GRI 3.0 reaction mechanism that contains 53 species and 325 reactions. The reduction of computational cost that can be achieved with a reduced mechanism is limited when using the SLFM, since neither the chemistry kinetics nor the transport equations for the species mass fractions have to solved in the LES. However, a significant saving is obtained in the cost for the evaluation of the

**Table 1** Extended Jones–Lindstedt mechanism of Frassoldati *et al.* [40] with Arrhenius coefficients: $k_f = AT^b \exp(E_A/(RT))$

| No. | Reaction | $A$ | $b$ | $E_A$, kcal/mol |
|---|---|---|---|---|
| 1 | $CH_4 + 0.5O_2 \Rightarrow CO + 2H_2$ | $3.06 \cdot 10^{10}$ | 0 | 30 |
| 2 | $CH_4 + H_2O \Rightarrow CO + 3H_2$ | $3.84 \cdot 10^{9}$ | 0 | 30 |
| 3 | $CO + H_2O \Rightarrow CO_2 + H_2$ | $2.01 \cdot 10^{9}$ | 0 | 20 |
| 4 | $H_2 + 0.5O_2 \Rightarrow H_2O$ | $8.06 \cdot 10^{16}$ | $-1$ | 40 |
| 5 | $O_2 \Rightarrow 2O$ | $1.5 \cdot 10^{9}$ | 0 | 113 |
| 6 | $H_2O \Rightarrow H + OH$ | $2.3 \cdot 10^{22}$ | $-3$ | 120 |

thermodynamic properties which increases with the number of species and constitutes a major proportion of the total run time in the present configuration.

The flamelets are generated using a strained counterflow diffusion flame configuration. Oxidizer and fuel are injected through opposed nozzles and form a diffusion flame in their midst. This configuration can be reduced to a one-dimensional problem along its centerline. Assuming unitary Lewis number for all species, the balance equations for species and temperature can be expressed in mixture fraction space as shown by Peters [23]:

$$\rho\frac{\partial Y_k}{\partial t} - \frac{1}{2}\,\rho\chi\frac{\partial^2 Y_k}{\partial f^2} - \dot{\omega}_k = 0\,; \tag{8}$$

$$\rho\frac{\partial T}{\partial t} - \frac{1}{2}\,\rho\chi\left(\frac{\partial^2 T}{\partial f^2} + \frac{1}{c_p}\,\frac{\partial c_p}{\partial f}\,\frac{\partial T}{\partial f}\right) + \frac{1}{c_p}\sum_{k=1}^{n} h_k\dot{\omega}_k = 0 \tag{9}$$

where $Y_k$ and $h_k$ are the mass fraction and the enthalpy of specie $k$, respectively. The laminar flamelets are generated with the Flamemaster software of Pitsch [41] under the assumption that the fluid is an ideal gas. As shown by Pohl *et al.* [42] or Kim *et al.* [43], this simplification has no significant effect on the species composition in the flamelet result. Finally, the filtered values of species mass fractions, which are used in the LES, are calculated using a $\beta$-shape PDF for the mixture fraction to account for SGS fluctuations:

$$\tilde{Y}_k\left(\tilde{f}, \widetilde{f''^2}, \tilde{\chi}_{\mathrm{st}}\right) = \int_0^1 Y_k\left(f^*; \tilde{\chi}_{st}\right) P\left(f^*; \tilde{f}, \widetilde{f''^2}\right)\, df^*\,.$$

These quantities, along with the transported fields and the thermodynamic models presented in subsection 2.2, provide a full representation of the LES flow field. Note that SGS fluctuations of $\tilde{\chi}$ are not considered here, since their influence on the simulation results is negligible. This becomes clear considering that the strain level in the LES is far from the extinction limit and changes in $\chi$, therefore, have a very limited effect on the flame structure. Furthermore, the scalar dissipation rate at stoichiometry $\tilde{\chi}_{\mathrm{st}}$ was approximated with its unconditioned value obtained from Eq. (6).

Figure 2 shows the result of a $CH_4/O_2$ flamelet simulation at $\chi_{\mathrm{st}} \approx 0$ and $p = 5.61$ MPa. The temperature boundary condition corresponds to the experimental operating conditions of Singla *et al.* [18]. To verify that the simplified reaction mechanism of Frassoldati *et al.* [40] is appropriate for the present configuration, the results are compared with a flamelet simulation using the full $CH_4/O_2$ reaction mechanism (GRI 3.0 [44]). Only minor differences can be observed. This is also reflected in Fig. 3 where the maximum temperature of a flamelet solution is plotted against the respective scalar dissipation rate. The extinction limit is $\chi_{\mathrm{st}}^{\mathrm{ext}} \approx 6 \cdot 10^5\ \mathrm{s}^{-1}$ for the full mechanism and $\chi_{\mathrm{st}}^{\mathrm{ext}} \approx 8 \cdot 10^5\ \mathrm{s}^{-1}$ for the mechanism of Frassoldati *et al.* [40].

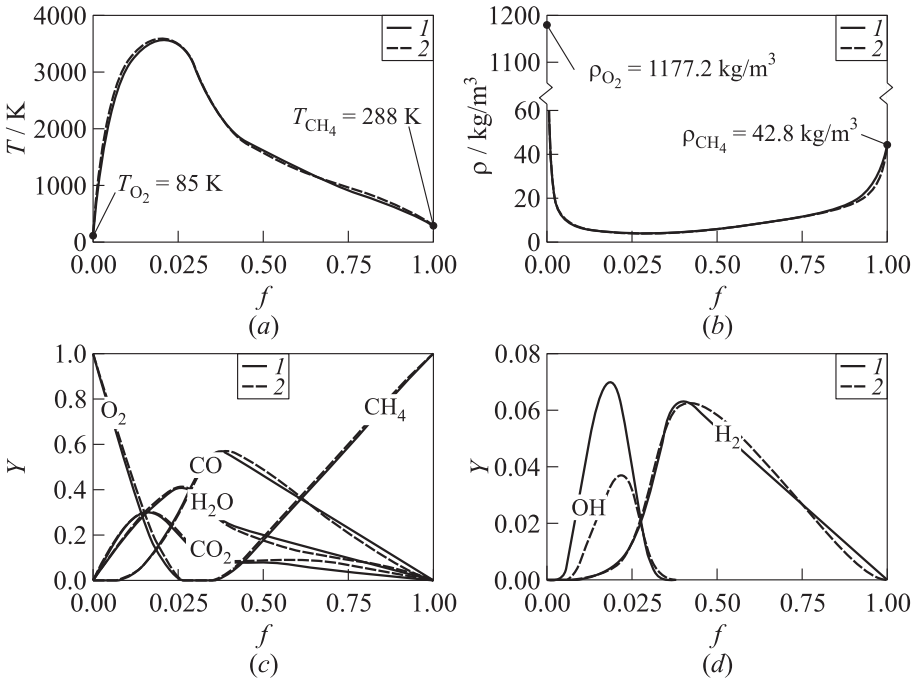


**Figure 2** $CH_4/O_2$ flamelet solution for $\chi_{st} \approx 0$ and $p = 5.61$ MPa: (*a*) temperature; (*b*) density; (*c*) major species; (*d*) minor species; *1* — full mechanism (GRI 3.0); and *2* — reduced mechanism of Frassoldati *et al.* [40]

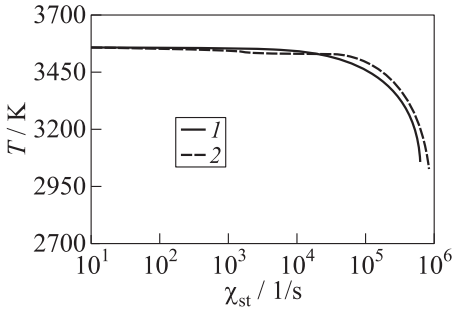


**Figure 3** Maximum temperature of a $CH_4/O_2$ flamelet solution at $p = 5.61$ MPa over scalar dissipation rate: *1* — full mechanism (GRI 3.0); and *2* — reduced mechanism of Frassoldati *et al.* [40]

# 3 EXPERIMENTAL AND NUMERICAL SETUP

## 3.1 Reference Experiment

The present numerical approach to simulate real-gas combustion is tested against the experiments of Singla *et al.* [18] who conducted $OH^*$ and $CH^*$ measurements for a series of trans- and supercritical $LOx/CH_4$ flames. The experiments were carried out at the well-known Mascotte testing facility [5, 45]. In the present configuration, oxygen is injected through an inner tube of a coaxial injector. The chamber is a $50 \times 50$ mm square duct with a length of 400 mm.

Singla *et al.* [18] performed several experiments varying both the chamber pressure and the injection temperature. For the present study, the authors simulate the operating point G2 for which the injection conditions are summarized in Table 2. The chamber pressure is supercritical with respect to the pure species ($p_{c,\,O_2} = 5.04$ MPa and $p_{c,\,CH_4} = 4.6$ MPa). The temperature of oxygen is cryogenic ($T_{O_2} = 85$ K) and the fluid is thus in a liquid-like state, which is characterized by a high density and viscosity. Methane is injected at ambient temperature ($T_{CH_4} = 288$ K) and features a much smaller, gas-like density.

**Table 2** Experimental injection conditions of Singla *et al.* [18] for operation point G2

| $p$, MPa | $T_{O_2}$, K | $T_{CH_4}$, K | $\dot{m}_{O_2}$, g/s | $\dot{m}_{CH_4}$, g/s | $\rho_{O_2}$[1], kg/m$^3$ | $\rho_{CH_4}$[1], kg/m$^3$ |
|---|---|---|---|---|---|---|
| 5.61 | 85 | 288 | 44.4 | 143.1 | 1177.2 | 42 |

[1] Calculated using NIST [36].

## 3.2 Computational Setup

The LES is performed with the open-source CFD (computational fluid dynamics) software OpenFOAM which is extended by the real-gas thermodynamics and combustion model described above.

Figure 4*a* shows the computational domain that is used for the present simulations. For the LES, the authors resolve the full cross section; however, the length of the computational domain is shortened to 150 mm. This is sufficient to accommodate the flame and avoid interference with the outlet. The grid contains $16 \cdot 10^6$ cells.

For the computations, the injector inner diameter is $D = 4.4$ mm. Methane is injected through an annulus with a slot width of 2.2 mm and an outer diameter of 10 mm. A detailed view of the grid around the injector is shown in Fig. 4*b*.

The turbulent inflow data for both $O_2$ and $CH_4$ are generated with a separate precursor incompressible LES using cyclic boundary conditions in axial direction.

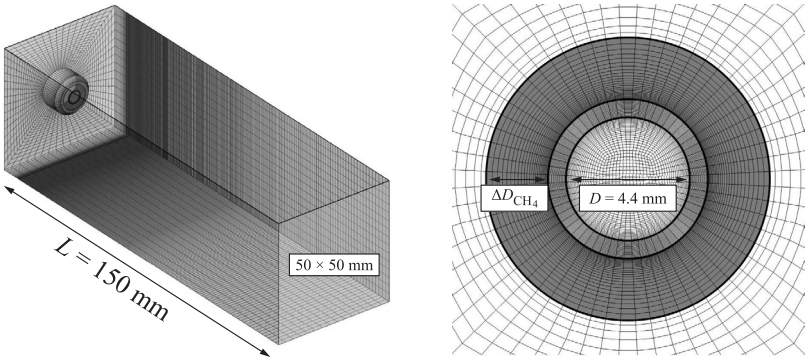


**Figure 4** Numerical domain: (*a*) computational domain; and (*b*) detailed view of the injector. Note that the grid was coarsened in the plot by a factor of two in each direction to avoid interference patterns

The domain length for these simulations is $L = 2\pi D_h$ where $D_h$ is the hydraulic diameter. Slices of the turbulent velocity fields are extracted from this simulation and accumulated in a database which is then used to interpolate the turbulent velocity field onto the coarser grids of the flame simulation.

For spatial discretization, a second-order central differences scheme with a van Leer limiter for momentum and scalar transport has been used to avoid unphysical oscillations. An implicit Euler scheme has been used for temporal discretization. To guarantee a stable evolution of the flow field, it was necessary to apply artificial dissipation in the mixture fraction and energy equation. The amount of dissipation is proportional to the local gradient of the compressibility factor and thus confined to regions of high-density gradient. The formulation essentially follows the work of Kawai *et al.* [46].

# 4 RESULTS

## 4.1 Instantaneous Flowfield

Figure 5 shows an instantaneous realization of the isocontour of the stoichiometric mixture fraction, i. e., $\tilde{f}_{\mathrm{st}} \approx 0.2$, demonstrating the location and dynamics of the jet flame. The color on the isosurface represents the velocity magnitude. Coherent vortices evolve rather close to the injector exit ($x/D \approx 1$) and grow quickly thereafter leading to fully turbulent conditions further downstream. The scales of turbulence grow until a strong radial expansion of the stoichio-

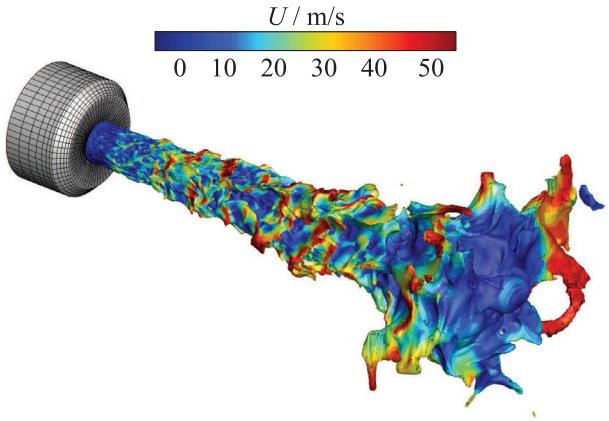


**Figure 5** Instantaneous realization of the stoichiometric mixture fraction isocontour ($\tilde{f}_{\mathrm{st}} = 0.2$)

metric mixture fraction isosurface can be observed that marks the end of the flame.

This particular flame shape can also be observed in Fig. 6 where snapshots of various flow properties in a plane perpendicular to the injector exit are shown. As indicated, for instance, by the temperature contour in Fig. 6*a*, the flame expands in the radial direction until $x \approx 60$ mm where reactions stop abruptly. It can also be observed that pockets of hot combustion products are transported towards the chamber walls where they are redirected either in the upstream or downstream direction. This can also be seen in Fig. 6*b*, where the axial velocity component is shown. The white isoline marks $\tilde{U}_x = 0$ m/s and encloses the recirculation zones. Besides the two backflow regions at the wall, upstream of the flame tip, a secondary region forms in the wake of the flame. This particular feature of the present configuration imposes a momentum on the flame tip in the upstream direction and thus intensifies the radial expansion at this position. This has also been observed by Schmitt *et al.* [20].

Figure 6*c* shows the instantaneous mixture fraction field which is used to access the flamelet library, the corresponding SGS variance is shown in Fig. 6*d*. The highest values of $\widetilde{f''^2}$ can be observed in the shear layer close to the injector exit plane and reach values in the order of $\sim 0.03$. Figure 6*e* shows the density field and demonstrates the conical shape of the dense oxygen core. Its surface is smooth when compared to the turbulent structures in the regions where the density is lower, e. g., the mixture fraction isosurface shown in Fig. 5. The compressibility factor $Z = pv/(RT)$, which is shown in Fig. 6*f*, is a measure for the thermodynamic nonideality of the mixture. The value $Z = 1$ corresponds to ideal gas behavior.

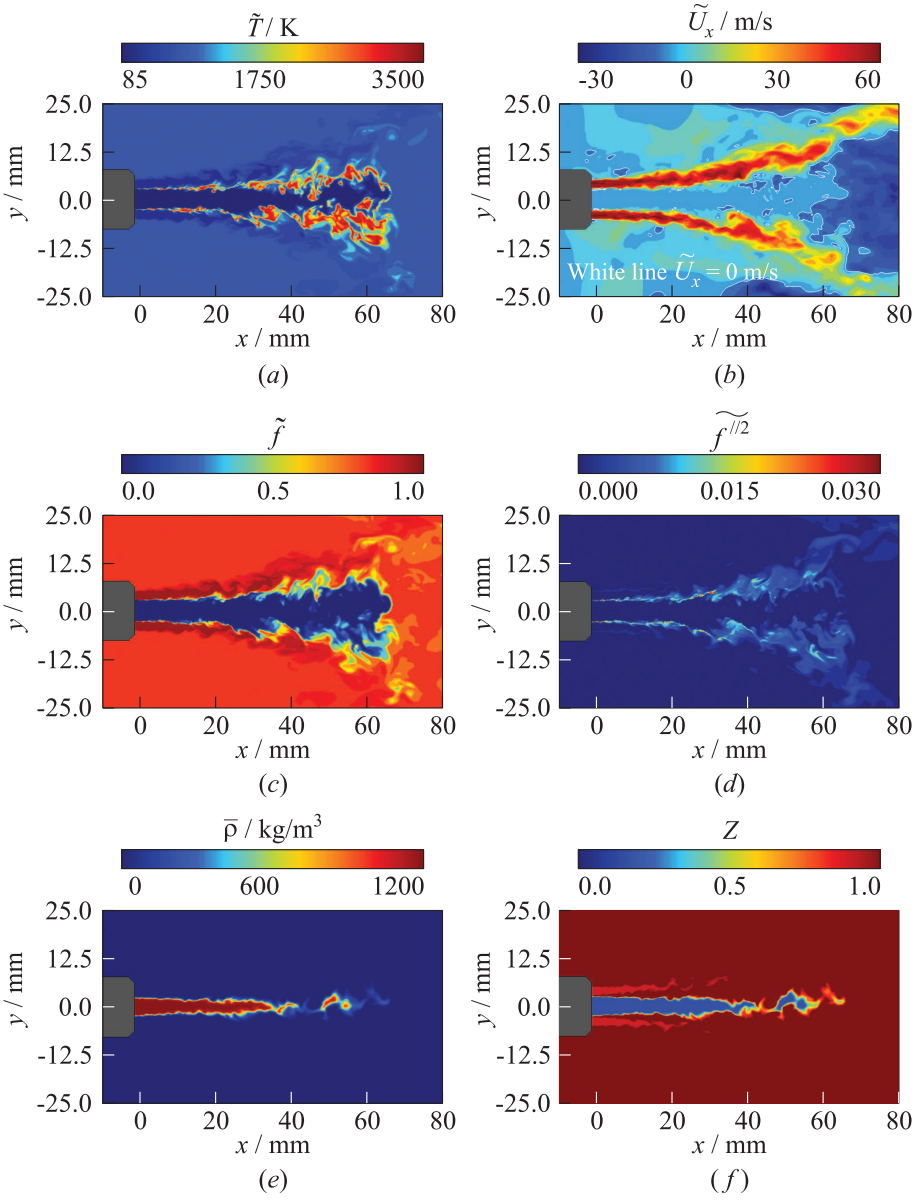


**Figure 6** Instantaneous realizations in a plane perpendicular to the inflow plane: (*a*) temperature; (*b*) axial velocity component; (*c*) mixture fraction; (*d*) mixture fraction variance; (*e*) density; and (*f*) compressibility factor

### 4.2 Averaged Flowfield

Temporal averaging was started after the flow field was considered fully developed in the region of interest and then continued for $\Delta t = 0.01$ s $\approx 10D/\bar{U}_{O_2}$. In addition, we make use of the symmetry and spatially average the flow field using the 4 half planes that are perpendicular to the injector plane and the chamber wall. The averaged OH mass fraction is compared with the experimental result of Singla *et al.* [18] in Fig. 7*a*. The predicted flame length is in good agreement with the experiment. Also, the flame shape, especially the expansion at $x \approx 60$ mm and the abrupt end of the flame, is well captured by the present simulations.

It is common practice to compare the numerical result for OH mass fraction or heat release rate with the measured radiation of the OH radical, henceforth referred to as OH*. Under certain conditions, this can be misleading as shown by Fiala and Sattelmayer [47]. They propose *a posteriori* method for numerical simulations to compute the OH* radiation under the assumption that OH and OH* are in thermal equilibrium:

$$c_{\mathrm{OH}^*} = c_{\mathrm{OH}} \exp\left(\frac{-\Delta g^0_{mf}}{RT}\right)$$

where $\Delta g^0_{mf}$ is the difference in the molar Gibbs standard state enthalpy of formation and is approximated as $\Delta g^0_{mf} = hcN_A/\lambda$ where $h$, $c$, and $N_A$ are the Planck constant, the speed of light, and the Avogadro constant, respectively.

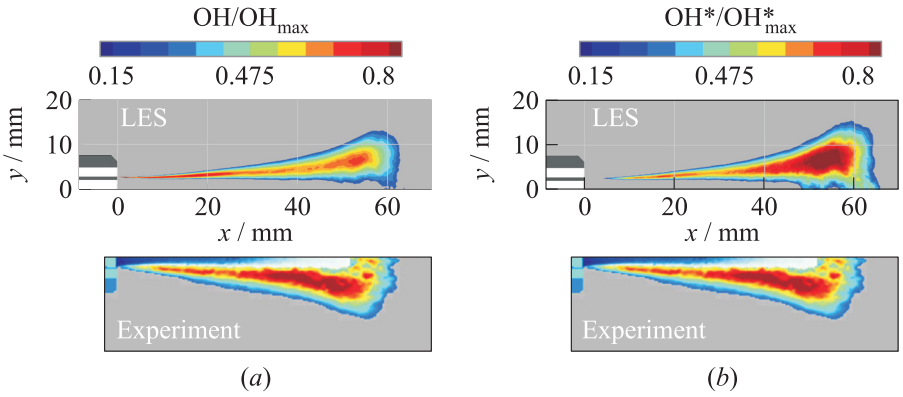


**Figure 7** Averaged OH (*a*) and OH* (*b*) mass fractions in comparison with the measured OH* (reprinted from Singla *et al.* [18, Fig. 4*d*]. Copyright 2004 The Combustion Institute. Published by Elsevier Inc.). Note that the color scale refers only to the numerical results

According to Fiala and Sattelmayer [47], $\lambda = 308$ nm is a good approximation for the representative wavelength.

The $OH^*$ radiation is computed at every time step and is averaged to obtain the correct statistics. Figure 7*b* shows the comparison with the measurements of Singla *et al.* [18]. The qualitative observations made above do not change, however, comparing the computed OH and the $OH^*$, we find that the location of the maximum value has shifted. While being located in the first section for the OH field, it is located further downstream for $OH^*$. This is in better agreement with the experimental result. Furthermore, the $OH^*$ field is detached from the injector post and stretches further downstream.

## 5 CONCLUDING REMARKS

The current contribution presents a modeling framework for LES of nonpremixed combustion at supercritical pressures. The main challenges are the accurate representation of thermodynamic nonidealities as well as of turbulent combustion. For the latter, we use a steady laminar flamelet approach assuming that the chemical reactions are fast compared to the turbulent mixing time scales. Subgrid fluctuations are taken into account using a $\beta$-shape PDF.

A reduced methane reaction mechanism that consists of 9 species and 6 reactions has been compared with the full mechanism, demonstrating its suitability for the particular operating conditions studied herein. The thermodynamic model consists of a cubic PR EoS and a volume-translation method that corrects deficiencies of the PR EoS at low temperatures. This method yields a highly accurate thermal EoS at reasonable computational effort.

Large-eddy simulations were performed for the experimental test case G2 of Singla *et al.* [18], in which LOx and $GCH_4$ are injected into a rectangular combustion chamber. The pressure is supercritical. A comparison with the available $OH^*$ radiation measurements showed that the predicted flame length is in good agreement with the experiment. Also, the characteristic expansion in the rear part of the flame is reproduced.

In addition, the LES result has been used to examine the difference between the OH mass fraction and the $OH^*$ radiation, which was computed with *a posteriori* method assuming thermal equilibrium between OH and $OH^*$. The result showed that the difference is not negligible for the present conditions.

## ACKNOWLEDGMENTS

Financial support has been provided by the German Research Foundation (DFG, Deutsche Forschungsgemeinschaft) in the framework of the Sonderforschungsbereich Transregio 40.

## REFERENCES


1. Mayer, W., and H. Tamura. 1996. Propellant injection in a liquid oxygen / gaseous hydrogen rocket engine. *J. Propul. Power* 12(6):1137–1147.
2. Mayer, W., A. Schik, B. Vielle, C. Chaveau, I. Gökalp, and D. Talley. 1998. Atomization and breakup of cryogenic propellants under high pressure subcritical and supercritical conditions. *J. Propul. Power* 14(5):835–842.
3. Oschwald, M., J. J. Smith, R. Branam, J. Hussong, A. Schik, B. Chehroudi, and D. Talley. 2006. Injection of fluids into supercritical environments. *Combust. Sci. Technol.* 178(1-3):49–100.
4. Chehroudi, B. 2012. Recent experimental efforts on high-pressure supercritical injection for liquid rockets and their implications. *Int. J. Aerospace Eng.* 2012:121802. 31 p.
5. Habiballah, M., M. Orain, F. Grisch, L. Vingert, and P. Gicquel. 2006. Experimental studies of high-pressure cryogenic flames on the Mascotte facility. *Combust. Sci. Technol.* 178(1-3):101–128.
6. Oefelein, J. C., and V. Yang. 1998. Modeling high-pressure mixing and combustion processes in liquid rocket engines. *J. Propul. Power* 14(5):843–857.
7. Zong, N., H. Meng, S.-Y. Hsieh, and V. Yang. 2004. A numerical study of cryogenic fluid injection and mixing under supercritical conditions. *Phys. Fluids* 16(12):4248–4261.
8. Oefelein, J. C. 2006. Mixing and combustion of cryogenic oxygen–hydrogen shear-coaxial jet flames at supercritical pressure. *Combust. Sci. Technol.* 178:229–252.
9. Matheis, J., H. Müller, C. Lenz, M. Pfitzner, and S. Hickel. 2016. Volume translation methods for real-gas computational fluid dynamics simulations. *J. Supercrit. Fluid.* 107:422–432.
10. Harstad, K. G., R. S. Miller, and J. Bellan. 1997. Efficient high-pressure state equations. *AIChE J.* 43(6):1605–1610.
11. Frey, K., M. Modell, and J. W. Tester. 2009. Density-and-temperature-dependent volume translation for the SRK EOS: 1. Pure fluid. *Fluid Phase Equilibria* 279:56–63.
12. Peng, D.-Y., and D. B. Robinson. 1976. A new two-constant equation of state. *Ind. Eng. Chem. Fundam.* 15:59–54.
13. Soave, G. 1972. Equilibrium constants from a modified Redlich-Kwong equation of state. *Chemical Engineering Sci.* 27:1197–1203.
14. Abudour, A. M., S. A. Mohammad, R. L. Robinson, Jr., and K. A. M. Gasem. 2013. Volume-translated Peng–Robinson equation of state for liquid densities of diverse binary mixtures. *Fluid Phase Equilib.* 349:37–55.
15. Chou, G. F., and J. M. Prausnitz. 1989. A phenomenological correction to an equation of state for the critical region. *AIChE J.* 35(9):1487–1496.
16. Müller, H., C. A. Niedermeier, J. Matheis, M. Pfitzner, and S. Hickel. 2016. Large-eddy simulation of nitrogen injection at trans- and supercritical conditions. *Phys. Fluids* 28(1):15102.

17. Müller, H., M. Pfitzner, J. Matheis, S. Hickel, M. Pfitzner, and S. Hickel. 2016. Large-eddy simulation of coaxial $LN_2/GH_2$ injection at trans- and supercritical conditions. *J. Propul. Power* 32(1):46–56.
18. Singla, G., P. Scouflaire, C. Rolon, and S. Candel. 2005. Transcritical oxygen/transcritical or supercritical methane combustion. *Proc. Combust. Inst.* 30:2921–2928.
19. Guezennec, N., M. Masquelet, and S. Menon. 2012. Large eddy simulation of flame–turbulence interactions in a LOx–$CH_4$ shear coaxial injector. AIAA Paper No. 2012-1267.
20. Schmitt, T., Y. Méry, M. Boileau, and S. Candel. 2011. Large-eddy simulation of oxygen/methane flames under transcritical conditions. *Proc. Combust. Inst.* 33(1):1383–1390.
21. Cutrone, L., P. De Palma, G. Pascazio, and M. Napolitano. 2010. A RANS flamelet-progress-variable method for computing reacting flows of real-gas mixtures. *Comput. Fluids* 39(3):485–498.
22. Kim, T., Y. Kim, and S. K. Kim. 2013. Effects of pressure and inlet temperature on coaxial gaseous methane/liquid oxygen turbulent jet flame under transcritical conditions. *J. Supercrit. Fluid.* 81:164–174.
23. Peters, N. 1984. Laminar diffusion flamelet models in non-premixed turbulent combustion. *Prog. Energ. Combust. Sci.* 10(3):319–339.
24. Peters, N. 2000. *Turbulent combustion.* Cambridge University Press. 304 p.
25. Zong, N., G. Ribert, and V. Yang. 2008. A flamelet approach for modeling of liquid oxygen LOx/methane flames at supercritical pressures. AIAA Paper No. 2008-946.
26. Ribert, G., N. Zong, V. Yang, L. Pons, N. Darabiha, and S. Candel. 2008. Counterflow diffusion flames of general fluids: Oxygen/hydrogen mixtures. *Combust. Flame* 154(3):319–330.
27. Garnier, E., N. Adams, and P. Sagaut. 2009. *Large eddy simulation for compressible flows.* Scientific computation ser. Springer Netherlands. 285 p.
28. Kemenov, K. A., H. Wang, and S. B. Pope. 2012. Modelling effects of subgrid-scale mixture fraction variance in LES of a piloted diffusion flame. *Combust. Theor. Model.* 16(4):611–638.
29. Vreman, A. W. 2004. An eddy-viscosity subgrid-scale model for turbulent shear flow: Algebraic theory and applications. *Phys. Fluids* 16(10):3670–3681.
30. Issa, R. I. 1986. Solution of the implicitly discretised fluid flow equations by operator-splitting. *J. Comput. Phys.* 93(2):40–65.
31. Issa, R. I., B. Ahmadi-Befrui, K. R. Beshay, A. D. Gosman, and A. Grosman. 1991. Solution of the implicitly discretised reacting flow equations by operator-splitting. *J. Comput. Phys.* 93(2):388–410.
32. Jarczyk, M., and M. Pfitzner, 2012. Large eddy simulation of supercritical nitrogen jets. AIAA Paper No. 2012-1270.
33. Goos, E., A. Burcat, and B. Ruscic. 2009. Extended third millennium ideal gas and condensed phase thermochemical database for combustion with updates from active thermochemical tables. Available at: http://burcat.technion.ac.il/dir (accessed August 24, 2017).

34. Poling, B. E., J. M. Prausnitz, and J. P. O'Connell. 2001. *The properties of gases and liquids*. 5th ed. McGraw-Hill Co. 706 p.
35. Chung, T.-H., M. Ajlan, L. L. Lee, and K. E. Starling. 1988. Generalized multiparameter correlation for nonpolar and polar fluid transport properties. *Ind. Eng. Chem. Res.* 27(4):671–679.
36. National Institute of Standards and Technology. 2017. Thermophysical properties of fluid systems. Available at: http://webbook.nist.gov/chemistry/fluid/ (accessed August 24, 2017).
37. Pons, L., N. Darabiha, and S. Candel. 2008. Pressure effects on nonpremixed strained flame. *Combust. Flame* 152(1-2):218–229.
38. Lacaze, G., and J. C. Oefelein. 2012. A non-premixed combustion model based on flame structure analysis at supercritical pressures. *Combust. Flame* 159(6):2087–2103.
39. Jones, W. P., and R. P. Lindstedt. 1988. Global reaction schemes for hydrocarbon combustion. *Combust. Flame* 73(3):233–249.
40. Frassoldati, A., A. Cuoci, T. Faravelli, E. Ranzi, C. Candusso, and D. Tolazzi. 2009. Simplified kinetic schemes for oxy-fuel combustion. *1st Conference (International) on Sustainable Fossil Fuels for Future Energy*. 6–10.
41. Pitsch, H. 2016. Flamemaster. Available at: http://www.itv.rwth-aachen.de/downloads/flamemaster/ (accessed August 24, 2017).
42. Pohl, S., M. Jarczyk, M. Pfitzner, and B. Rogg. 2013. Real gas CFD simulations of hydrogen/oxygen supercritical combustion. *Progress in propulsion physics*. Eds. L. T. DeLuca, C. Bonnal, O. Haidn, and S. M. Frolov. EUCASS advances in aerospace sciences book ser. TORUS PRESS – EDP Sciences. 4:583–614.
43. Kim, T., Y. Kim, and S.-K. Kim. 2011. Real-fluid flamelet modeling for gaseous hydrogen/cryogenic liquid oxygen jet flames at supercritical pressure. *J. Supercrit. Fluids* 58(2):254–262.
44. Smith, G. P., D. M. Golden, M. Frenklach, N. W. Moriarty, B. Eiteneer, M. Goldenberg, C. T. Bowman, R. K. Hanson, S. Song, W. C. Gardiner, V. V. Lissianski, and Z. Qin. GRI-Mech. Available at: http://www.me.berkeley.edu/gri_mech/ (accessed August 24, 2017).
45. Candel, S., G. Herding, R. Snyder, P. Scouflaire, C. Rolon, L. Vingert, M. Habiballah, F. Grisch, M. Péalat, P. Bouchardy, D. Stepowski, A. Cessou, and P. Colin. 1998. Experimental investigation of shear coaxial cryogenic jet flames. *J. Propul. Power* 14(5):826–834.
46. Kawai, S., S. K. Shankar, and S. K. Lele. 2010. Assessment of localized artificial diffusivity scheme for large-eddy simulation of compressible turbulent flows. *J. Comput. Phys.* 229(5):1739–1762.
47. Fiala, T., and T. Sattelmayer. 2013. *A posteriori* computation of OH* radiation from numerical simulations in rocket combustion chambers. *5th European Conference for Aeronautics and Space Sciences (EUCASS)*.